A Coordination-Based Model for Transition Metal Alloy Nanoparticles

Journal:	*Nanoscale*
Manuscript ID	NR-ART-01-2019-000959
Article Type:	Paper
Date Submitted by the Author:	29-Jan-2019
Complete List of Authors:	Roling, Luke; Iowa State University, Department of Chemical & Biological Engineering Choksi, Tej; Stanford University, Chemical Engineering Abild-Pedersen, Frank; Stanford Linear Accelerator Center, SunCat

SCHOLARONE™
Manuscripts

A Coordination-Based Model for Transition Metal Alloy Nanoparticles

Luke T. Roling[1#], Tej S. Choksi[1#], and Frank Abild-Pedersen[2*]

[1]SUNCAT Center for Interface Science and Catalysis, Department of Chemical Engineering, Stanford University, Stanford, CA 94305, USA

[2]SUNCAT Center for Interface Science and Catalysis, SLAC National Accelerator Laboratory, 2575 Sand Hill Road, Menlo Park, California 94025, USA

[#] These authors contributed equally to this work.
[*]Corresponding Author
E-mail: abild@slac.stanford.edu

Abstract

We present a simple approach for predicting the relative energies of bimetallic nanoparticles spanning a wide-ranging combinatorial space, using only the identity and nearest-neighbor coordination number of individual metal atoms as independent parameters. By performing straightforward metal atom adsorption calculations on surface slab models, we parameterize expressions for the energy of metal atoms as a function of their coordination number in 21 bimetallic pairings of fcc metals. We rigorously establish the transferability of our model by predicting relative energies of a series of nanoparticles across a large number of morphologies, sizes, atomic compositions, and arrangements. The model is particularly accurate in predicting atomic rearrangements at or near the metal surfaces, which is essential for its potential applications when studying segregation phenomena or dynamic processes in heterogeneous catalysis. By rapidly forecasting site stabilities with atomic specificity across generic structural and compositional features, our model is able to reverse engineer thermodynamically feasible motifs of active sites in bimetallic nanoparticles through robust property $\Leftrightarrow$ structure relations.

Introduction

Alloy nanoparticles are widely used in heterogeneous catalytic applications, and are synthesized to take advantage of desirable additive or synergistic properties of the component metals.[1–3] Relative to their monometallic counterparts, alloy nanoparticle systems are characterized by a large number of atomic arrangements in configurational space which presents a formidable computational challenge in efficiently screening across materials space. Experimental measurements of surface segregation are feasible on a system-by-system basis,[4,5] but lack the complete site-by-site, atomic-scale resolution that can be realized from first-principles calculations. It is therefore highly desirable to develop an efficient computational framework for predicting the energies of bimetallic systems based on their surface structure, size, and composition. Such an understanding will ultimately enable identification of realistic nanoparticle structures and their morphological evolution under catalytic conditions. Furthermore, the integration of such a framework with traditional volcano-based reactivity maps would enable targeted screening of thermodynamically feasible active site ensembles as a function of their morphology and local chemical environment.

A number of efforts have been made to understand the ordering properties of bimetallic systems.[6,7] Early computational studies predicted surface segregation phenomena in various dilute slab-based models using quantum chemical calculations.[8,9] More recent electronic structure calculations have looked at phenomena involving surface growth[10,11] or using more complex nanoparticle models.[12–14] A variety of methods have attempted to generalize these ordering principles, including the use of neural networks[15–17], Bayesian linear regression[18,19], cluster expansions[20], and genetic algorithms[21–24], among others.[25–28] We also note that the surface ordering of alloys is highly dependent on catalytic reaction conditions, and that the

presence of intermediates in a catalytic reaction can strongly influence both the catalyst shape and the segregation of metal components to the surface.[29–32] Although promising, these methods have been applied to a specific alloy composition, e.g. Rh/Au[18,19] or Ni/Fe[20], and need to be refitted using several hundred additional calculations for each new system. Notwithstanding the predictive power of model parameters like weight factors (Bayesian regressions) or effective cluster interactions (cluster expansion), a physical interpretation of obtained parameter values still remains elusive. Despite these recent developments, an alloy stability model that can be generalized across the immense materials space spanning bimetallic nanoalloys but using only a limited number of physically meaningful parameters is currently lacking. We postulate an alternative framework for predicting the relative ordering of generic alloy structures based on parameterizing the energy of constituent atoms as a function of their coordination number. Our model is motivated by screening effects of itinerant transition metal d-electrons that largely confine perturbations in coordination or composition to a region of one lattice constant[33]. We show that this phenomenon greatly decreases the number of parameters required to efficiently describe generic morphologies and compositions of bimetallic nanoparticles.

We previously presented a method for determining the energies of individual metal atoms in monometallic systems based solely on the metal identity and their individual coordination to other metal atoms using a small set of simple density functional theory (DFT) calculations.[34] By tracking changes in atomic coordination corresponding to metal atom adsorption events on surface slab models, the adsorption energies of metal atoms could be predicted in a more general configurational space (*e.g.* nanoparticles). This model was particularly successful in determining the relative ordering of nanoparticles with varying atomic arrangements, which is critically important when identifying minimum energy structures and for applications in dynamic

simulations (*e.g.*, kinetic Monte Carlo simulations of sintering).[35] We also subsequently identified simple mappings between energies of metal configurations and the adsorption energies of catalytic intermediates on monometallic systems, which suggests extension of these dynamic simulations to systems under catalytic operating conditions.[36] Although such an extension to adsorbate-induced segregation is outside the scope of the present work, this recent work provides a framework by which such effects could be addressed through relations between molecular adsorption energies and the stability of the metal site to which they bind.

In this study, we show that a coordination-based model that considers compositional variations through a mean field approach can predict relative energies of atomic arrangements for both periodic surfaces and nanoparticle models across 21 binary pairings of Ag, Au, Cu, Ir, Pd, Pt, and Rh with high accuracy. In contrast with previous approaches, this framework is transferable to a number of nanoalloys having different sizes, morphologies, and overall compositions, and is highly efficient since it only requires a relatively small number of DFT calculations to fit a limited number of parameters. This approach will enable accurate and efficient future simulations of the evolution of metal nanoparticles as a function of shape, composition, and (ultimately) the reaction environment, *i.e.*, the chemical potential of reactive species. Moreover, by rapidly screening site stabilities, our framework is capable of reverse engineering the morphology of realistic active site ensembles, ultimately enabling the inverse design of bimetallic alloy catalysts.

Computational methods

Density functional theory (DFT) calculations were performed using the same framework as in our previous work.[34] The Quantum ESPRESSO[37] software package was used with the RPBE functional[38] and ultra-soft Vanderbilt pseudopotentials[39] within the atomic simulation

environment (ASE).[40] Kinetic energy cutoffs of 500 eV for plane waves, and 5000 eV for charge densities were used. We performed calculations on seven fcc transition metals, however, because of the generality of these coordination-based concepts we note that the approach should be transferable to transition metals with other crystal structures. Ni was omitted from our present analysis so as to avoid complications and additional computational costs associated with spin polarization; Ni was shown in our previous work[34] to follow the same principles as the other monometallic fcc systems, so we anticipate these concepts also should be extendable to Ni bimetallic systems. The lattice constants of metals in this study were optimized to the following values (experimental values[41] in parentheses, all values in Å): Ag 4.22 (4.09), Au 4.20 (4.08), Cu 3.68 (3.61), Ir 3.88 (3.84), Pd 3.98 (3.89), Pt 3.99 (3.92), Rh 3.85 (3.80).

Calculations on fcc(111) and fcc(100) surface geometries were performed with a base slab of six layers of metal atoms; the bottom four layers were fixed at their bulk-optimized coordinates and all other atoms were fully relaxed. Calculations on fcc(211) slab models were performed with a base slab of 12 layers, and the bottom six layers were fixed. At least 12 Å of vacuum separated successive slabs in the periodic z-direction. Partial occupancies were determined using a Fermi – Dirac smearing of 0.10 eV facilitating faster convergence of the Kohn – Sham equations. The dipole correction to the total energy was applied perpendicular to the slab for all surface calculations.[42] All calculations are spin-paired as the metals considered do not display magnetic ordering. Monkhorst-Pack k-point grids[43] were used for all calculations: 2 x 2 surface unit cells were sampled with 8 x 8 x 1 grids, and 3 x 3 surface unit cells were sampled with 6 x 6 x 1 grids. Calculations in 3 x 3 x 3 unit cells of bulk metals (*i.e.*, no vacuum) were performed with 6 x 6 x 6 k-point grids and all atoms relaxed. Considered nanoparticle morphologies include cuboctahedral (CUB), octahedral (OCT), decahedral (DEC), and

6

icosahedral (ICO) structures. Atomic coordinates of initial structures were obtained using ASE.[40] To understand the impact of finite size effects, we utilize 147 atom and truncated 309 atom (half-309) CUB nanoparticles. All atoms in the nanoparticle calculations were relaxed (unless otherwise noted) with at least 10 Å of vacuum spacing in all directions, using only the gamma point. For the half-309 nanoparticles, atoms in the bottom-most layer were fixed to their bulk positions. Gas phase energies were computed using spin polarized calculations in 21 Å x 22 Å x 23 Å unit cells, at planewave and density cutoffs of 500 eV and 5000 eV respectively. All geometry optimizations were performed with a force convergence criterion of 0.02 eV Å^{-1}.

In some cases of surface adsorption, particularly for large atoms (*e.g.* Au, Ag) adsorbed at higher coverage on surfaces with a smaller lattice (*e.g.* Cu), or stronger-binding metals (*e.g.* Ir, Rh) adsorbed on weaker-binding metals (Au, Ag), substantial corrugation or other deviations of the surface layer from ideal fcc stacking were observed. We chose to disregard energetics from these reconstructions from our analysis and subsequent parametrization, since the coordination number of atoms is much less clearly defined than in an ideal fcc stacking. The specific reconstruction criteria used to exclude data are: (1) deviations of more than 0.5 Å in the *z*-coordinate of atoms within any given metal layer, (2) nearest-neighbor interatomic distances within a layer greater than 1.05 times the equilibrium lattice interatomic distance, and/or (3) nearest-neighbor interatomic distances within a layer less than 0.9 times the equilibrium lattice interatomic distance. Applying these criteria, only 9% of all adsorption energies were excluded from the training set, including no more than 25% of adsorption energies obtained for any specific bimetallic combination.

Results and Discussion

We discuss the formulation, validation, and applications of our coordination-based model for bimetallic nanoparticles across five sections. We begin by postulating our coordination-based model for predicting site stabilities of monometallic catalysts.[34] We describe a scheme to efficiently treat compositional and structural variations across 21 different bimetallic pairings. In the second part, we evaluate our framework in depth on (111) surfaces of Pd-Pt alloys having compositions ranging from Pt rich to Pd rich. In the third section, we highlight the necessity of accounting for charge density accumulation on atoms within the first sublayer in bimetallic alloys. Next, we rigorously establish the transferability of our model in predicting both relative, and total energies of nanoparticles having wide ranging morphologies, compositions, and sizes. While analyzing the nanoparticle energies, we elucidate correction schemes that account for the destabilizing effect of charge density accumulation that is initially discussed in part three. Finally, we compare the accuracy, transferability, and computational cost of our paradigm to existing approaches for treating alloy nanoparticles and discuss the broader impact of this framework in understanding bimetallic catalysts.

A Coordination-Based Model for Bimetallic Systems

We first recount the important results of our model established in the context of monometallic adsorption calculations,[34] and subsequently formulate our scheme for efficiently treating bimetallic compositional space. The energy E_n^Z of a metal atom in a given configuration is determined only by its identity (Z) and coordination number (n) to nearest-neighbor atoms in an fcc lattice stacking, with $E_0^Z = 0$ (gas-phase atom) chosen as a reference state. This assumption arises from the inherent nearsightedness in transition metals where perturbations beyond one

lattice constant are dampened because of the itinerant nature of d-electrons.[33] The discrete set of E_n^Z for each metal is determined by assigning energies to each sequential coordination formed by a central atom to its nearest-neighbor atoms; these bond-associated energies are denoted as α_i^Z. The energy of an atom with a given coordination number is calculated as the sum of all α_i^Z up to that coordination number, *i.e.*, $E_n^Z = \sum_{i=1}^n \alpha_i^Z$. The individual parameters, α_i^Z, are determined through least-squares regression of metal atom adsorption energies to the corresponding changes in atomic coordination in both the metal atom and the metal surface (see a simple schematic in Figure 1). Since metal atom coordination of 1 or 2 is not explicitly considered within these calculations, we use one "lumped" parameter α_{1-3}^Z containing the first three bond-associated energies; this yields a total of 10 bond-associated energies $\{\alpha_{1-3}^Z, \alpha_4^Z,...,\alpha_{12}^Z\}$ for each metal considered. We showed that parameters derived in this manner from 14 simple adsorption calculations allowed accurate prediction of adsorption energies of metal atoms in larger surface unit cells, as well as on nanoparticle models. We also found that special attention was needed for the calculation of atomic energies for atoms located in the first subsurface layer; this was rationalized on the basis of subsurface charge accumulation due to the surface termination. We show explicitly how to apply these subsurface corrections to the bimetallic systems later in this work.
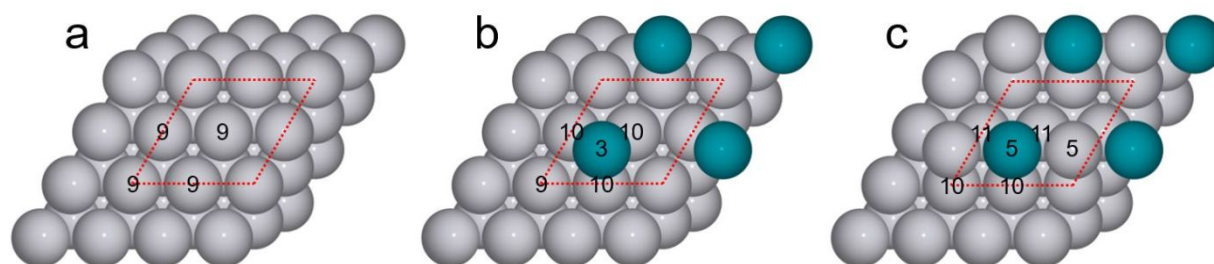
Figure 1: Schematic of changes in atomic coordination corresponding to sequential adsorption of metal atoms: (a) clean fcc(111) surface slab of metal B, (b) after addition of one atom of metal A, (c) after subsequent addition of one atom of metal B. The unit cell of the surface modeled is

indicated (red dashed line). The coordination number of surface atoms is shown. Metal A is shown in blue, and metal B in grey.

We now introduce compositional variations within the coordination-based framework by considering 21 possible bimetallic combinations of the seven fcc metals (Ag, Au, Cu, Ir, Pd, Pt, Rh). Our monometallic analysis considered 14 adsorption energies for each metal, which consisted of all unique sequential additions of metal atoms within the considered unit cell sizes and symmetry of (111), (100), and (211) surface terminations, along with a calculation of removing an atom from a bulk fcc lattice. We here consider the same sequence of metal adsorption energies within a 2 x 2 surface unit cell of (111) and (100) slab models, and within a 1 x 3 surface unit cell of (211) slab models. The introduction of a second metal on a given surface provides a composition degree of freedom and breaks symmetry to yield additional unique surface configurations. We therefore added metal atoms (of either species "A" or "B", generally) sequentially to fcc(111), fcc(100), and fcc(211) monometallic slabs of metal B to determine adsorption energies as a function of change in atomic coordination numbers; an example of such adsorptions is shown in Figure 1. These sequential adsorptions yield a surface layer composed of metals A and/or B on a slab of pure metal B. We also calculated the adsorption energy of one atom A or B in a 3 x 3 x 3 unit cell of bulk B. We note that up to four metal atoms may be added to form a complete adlayer in the 2 x 2 surface unit cells of fcc(111) and fcc(100) slabs, and up to three metal atoms to form an additional metal layer in the 1 x 3 surface unit cell of the fcc(211) slabs. By considering all permutations of adatoms A and B within these constraints, a total of 140 adsorption energies are computed for each bimetallic system (although, a small fraction of these is discarded during model parameterization in cases of substantial surface reconstruction with the specific criteria stated in the computational methods section).

These adsorption energies in bimetallic systems were used as the basis for a new model to predict the energies of bimetallic surface configurations, utilizing the same paradigm developed for monometallic systems: the energy E_n^Z of an atom is determined by its coordination number n and its identity Z, and is calculated as the sum of its corresponding bond-associated α_i^Z parameters. Notably, the energy of an atom depends only on the total coordination number in our model, and not on the atomic identity of its nearest neighbors. We note, however, that unlike E_n^Z, quantities such as the energetics of elementary processes (*e.g.*, adsorption, diffusion) are longer-range in nature because they are derived from changes in coordination (and energy) of both the atom under consideration and its nearest neighbors. Therefore, even though the energy assigned to a particular atom is defined only by its identity and its coordination number, the identity and coordination information about all its neighboring atoms is required to describe elementary processes involving movement of that central atom.

As a first test of this method, we attempted to describe adsorption energies in bimetallic systems using the parameters obtained from the monometallic analysis, *i.e.*, the energies of atoms of metal "A" were predicted as a function of the α_i^A parameters associated with metal A, and the energies of metal atoms "B" were determined by the α_i^B parameters associated with metal B from our previous work.[34] Thus, by neglecting perturbations caused by chemically disparate nearest neighbors, this formalism represents a limiting case where strong d-electron screening is assumed. The implications of this assumption, along with refinements to our model that introduce compositional variation in a mean field approach are discussed throughout the subsequent text. Discussions with an example prediction of metal adsorption energies using the monometallic parameters is provided in the ESI, and the full set of DFT-calculated adsorption energies is provided in Tables S1 – S8. The monometallic parameters are presented in the shaded

columns of Table 1, and summarized results of the accuracy of these predictions are given in

Table 2A-B. The average mean absolute error (MAE) across all 21 bimetallic combinations is

0.18 eV. The worst fits (MAE > 0.20 eV) were found for combinations across two columns of

the periodic table (*i.e.*, Ag/Au/Cu with Ir/Rh); remaining combinations were described with a

MAE of 0.13 eV. These results imply that d-electron screening in alloys composed of chemically

dissimilar elements are weaker and compositional effects need to be explicitly included within

α_i^Z parameters. Still, the overall magnitude of the error is relatively small, particularly

considering that only 98 monometallic calculations (14 for each metal) were used to predict over

2200 bimetallic adsorption energies (up to 140 for each bimetallic pairing, including the 28 total

adsorption energies for the monometallic components).

Table 1: Bond-associated α_i^Z parameters optimized for the bimetallic systems considered in this study. The values listed in each row are bond-associated parameters α_i^Z used to determine the energy of the listed metal Z, corresponding to bimetallic pairings of Z with the elements in each column. The parameters corresponding to monometallic systems are lightly shaded. All values are provided in eV.

	Ag	Au	Cu	Ir	Pd	Pt	Rh
α_{1-3}^{Ag}	-1.247	-1.375	-1.336	-1.271	-1.315	-1.421	-1.316
α_4^{Ag}	-0.118	-0.094	-0.129	-0.087	-0.124	-0.081	-0.096
α_5^{Ag}	-0.096	-0.102	-0.051	0.029	-0.083	-0.080	-0.006
α_6^{Ag}	-0.076	-0.089	-0.073	-0.079	-0.084	-0.093	-0.064
α_7^{Ag}	-0.091	-0.069	-0.055	-0.033	-0.095	-0.057	-0.057
α_8^{Ag}	-0.072	-0.060	-0.068	-0.059	-0.077	-0.077	-0.052
α_9^{Ag}	-0.074	-0.076	-0.043	-0.033	-0.077	-0.064	-0.030
α_{10}^{Ag}	-0.087	-0.070	-0.056	0.006	-0.081	-0.035	-0.020
α_{11}^{Ag}	-0.082	-0.067	-0.053	-0.025	-0.079	-0.047	-0.060
α_{12}^{Ag}	-0.058	-0.058	-0.043	-0.028	-0.056	-0.045	-0.046

	Ag	Au	Cu	Ir	Pd	Pt	Rh
α_{1-3}^{Pd}	-1.787	-1.905	-1.898	-2.005	-1.832	-2.049	-1.894
α_4^{Pd}	-0.250	-0.211	-0.282	-0.158	-0.237	-0.170	-0.225
α_5^{Pd}	-0.078	-0.093	-0.051	-0.064	-0.096	-0.103	-0.068
α_6^{Pd}	-0.160	-0.160	-0.155	-0.111	-0.141	-0.131	-0.123
α_7^{Pd}	-0.162	-0.134	-0.154	-0.118	-0.169	-0.130	-0.151
α_8^{Pd}	-0.145	-0.120	-0.133	-0.107	-0.146	-0.124	-0.132
α_9^{Pd}	-0.159	-0.164	-0.147	-0.125	-0.139	-0.128	-0.122
α_{10}^{Pd}	-0.163	-0.140	-0.150	-0.078	-0.138	-0.095	-0.110
α_{11}^{Pd}	-0.151	-0.144	-0.140	-0.115	-0.132	-0.114	-0.120
α_{12}^{Pd}	-0.100	-0.107	-0.098	-0.096	-0.100	-0.103	-0.096

	Ag	Au	Cu	Ir	Pd	Pt	Rh
α_{1-3}^{Au}	-1.830	-1.830	-1.943	-1.819	-1.756	-1.827	-1.832
α_4^{Au}	-0.125	-0.111	-0.117	-0.071	-0.139	-0.099	-0.089
α_5^{Au}	-0.105	-0.125	-0.100	-0.029	-0.138	-0.138	-0.091
α_6^{Au}	-0.084	-0.097	-0.045	-0.097	-0.090	-0.099	-0.057
α_7^{Au}	-0.092	-0.071	-0.094	-0.023	-0.119	-0.082	-0.084
α_8^{Au}	-0.059	-0.053	-0.023	-0.053	-0.066	-0.065	-0.028
α_9^{Au}	-0.081	-0.080	-0.059	-0.027	-0.092	-0.072	-0.051
α_{10}^{Au}	-0.068	-0.042	-0.049	0.043	-0.071	-0.016	-0.012
α_{11}^{Au}	-0.054	-0.033	-0.026	0.018	-0.046	-0.005	-0.024
α_{12}^{Au}	-0.034	-0.028	-0.021	0.002	-0.026	-0.011	-0.018

	Ag	Au	Cu	Ir	Pd	Pt	Rh
α_{1-3}^{Pt}	-3.071	-3.144	-3.286	-3.346	-3.146	-3.414	-3.253
α_4^{Pt}	-0.322	-0.303	-0.315	-0.230	-0.317	-0.228	-0.288
α_5^{Pt}	-0.124	-0.135	-0.184	-0.209	-0.190	-0.206	-0.205
α_6^{Pt}	-0.206	-0.214	-0.165	-0.141	-0.188	-0.157	-0.147
α_7^{Pt}	-0.221	-0.175	-0.239	-0.198	-0.236	-0.190	-0.237
α_8^{Pt}	-0.148	-0.128	-0.145	-0.103	-0.154	-0.116	-0.127
α_9^{Pt}	-0.224	-0.230	-0.206	-0.223	-0.219	-0.211	-0.225
α_{10}^{Pt}	-0.188	-0.157	-0.173	-0.112	-0.166	-0.111	-0.150
α_{11}^{Pt}	-0.139	-0.125	-0.106	-0.083	-0.111	-0.088	-0.103
α_{12}^{Pt}	-0.062	-0.064	-0.052	-0.051	-0.056	-0.056	-0.055

	Ag	Au	Cu	Ir	Pd	Pt	Rh
α_{1-3}^{Cu}	-1.799	-1.991	-1.750	-1.549	-1.922	-2.051	-1.764
α_4^{Cu}	-0.218	-0.161	-0.200	-0.203	-0.154	-0.148	-0.208
α_5^{Cu}	-0.069	-0.084	-0.112	-0.031	-0.097	-0.085	-0.062
α_6^{Cu}	-0.133	-0.158	-0.129	-0.105	-0.138	-0.153	-0.136
α_7^{Cu}	-0.123	-0.111	-0.159	-0.163	-0.144	-0.102	-0.136
α_8^{Cu}	-0.111	-0.074	-0.132	-0.139	-0.124	-0.096	-0.130
α_9^{Cu}	-0.113	-0.132	-0.132	-0.181	-0.140	-0.148	-0.139
α_{10}^{Cu}	-0.148	-0.142	-0.171	-0.213	-0.170	-0.142	-0.151
α_{11}^{Cu}	-0.140	-0.128	-0.153	-0.247	-0.163	-0.163	-0.170
α_{12}^{Cu}	-0.078	-0.088	-0.085	-0.088	-0.093	-0.106	-0.096

	Ag	Au	Cu	Ir	Pd	Pt	Rh
α_{1-3}^{Rh}	-2.668	-2.874	-2.858	-2.990	-2.886	-3.167	-2.942
α_4^{Rh}	-0.481	-0.439	-0.425	-0.392	-0.431	-0.353	-0.430
α_5^{Rh}	-0.159	-0.178	-0.205	-0.151	-0.148	-0.166	-0.148
α_6^{Rh}	-0.262	-0.255	-0.225	-0.226	-0.246	-0.225	-0.214
α_7^{Rh}	-0.258	-0.224	-0.268	-0.211	-0.233	-0.196	-0.241
α_8^{Rh}	-0.240	-0.204	-0.234	-0.197	-0.224	-0.180	-0.219
α_9^{Rh}	-0.232	-0.247	-0.244	-0.278	-0.245	-0.250	-0.261
α_{10}^{Rh}	-0.259	-0.239	-0.269	-0.270	-0.263	-0.237	-0.276
α_{11}^{Rh}	-0.211	-0.208	-0.220	-0.262	-0.231	-0.231	-0.258
α_{12}^{Rh}	-0.132	-0.145	-0.140	-0.167	-0.151	-0.162	-0.159

	Ag	Au	Cu	Ir	Pd	Pt	Rh
α_{1-3}^{Ir}	-3.222	-3.546	-3.387	-3.736	-3.638	-3.913	-3.671
α_4^{Ir}	-0.499	-0.576	-0.641	-0.501	-0.562	-0.502	-0.562
α_5^{Ir}	-0.382	-0.335	-0.261	-0.319	-0.291	-0.302	-0.296
α_6^{Ir}	-0.316	-0.304	-0.326	-0.271	-0.321	-0.310	-0.302
α_7^{Ir}	-0.357	-0.314	-0.351	-0.310	-0.322	-0.258	-0.338
α_8^{Ir}	-0.328	-0.252	-0.277	-0.252	-0.284	-0.226	-0.269
α_9^{Ir}	-0.360	-0.337	-0.386	-0.400	-0.335	-0.349	-0.376
α_{10}^{Ir}	-0.344	-0.293	-0.396	-0.365	-0.330	-0.298	-0.367
α_{11}^{Ir}	-0.256	-0.222	-0.297	-0.311	-0.254	-0.248	-0.295
α_{12}^{Ir}	-0.128	-0.134	-0.142	-0.160	-0.145	-0.154	-0.157

We refine our treatment of compositional effects by re-optimizing the 20 α_i^Z parameters (10 for each metal) for each of the 21 possible bimetallic systems. Using α_i^Z from the monometallic optimizations as initial guess values, we minimize the sum of squared residuals in the predicted bimetallic adsorption energies and generate a new set of α_i^Z parameters which

explicitly include interactions between binary pairs through a mean field approach. The α_i^Z parameters are fit to the set of up to 140 bimetallic adsorption energies (obtained from 96 DFT calculations on bulk, (100), (111), and (211) surfaces) using the coefficient arrays presented in Tables S9 – S12 and the adsorption energies in Tables S1 – S8. The optimized parameters for each bimetallic system are provided in Table 1. We note here that we choose to include the monometallic adsorption energies in determining these bimetallic parameter sets, so as to train the bimetallic parameters to the full composition range of 0-100% of metal A/B. Including these monometallic data aids our understanding of dilute systems and a general description of the full composition range; the parameter sets can in principle be improved and tuned by increasing sampling at a particular bimetallic ratio, though such an analysis is outside the scope of the present work. There are two physically meaningful trends among α_i^Z parameters in Table 1. First, as they represent gains in energy for each additional bond, α_i^Z parameters should have negative signs. We indeed observe this trend without adding additional constraints as only 5 out of 490 parameters across 21 bimetallic combinations, are small positive numbers. The exceptions (Ag/Ir and Au/Ir parameters) correspond to cases less relevant to real catalytic systems, as discussed subsequently for bimetallic pairings across two columns of the periodic table. Second, the differential gain in energy represented by α_i^Z parameters is anticipated to be greater (lower) for lower coordinated (higher coordinated) atoms. This trend is also manifested in Table 1 as α_i^Z parameters are typically more negative for lower coordination numbers.

We then used these parameters to reconstruct the adsorption energy set for each bimetallic system (example adsorption energy calculations are discussed in detail in the ESI), and compared the resulting values with the DFT-calculated adsorption energies; the MAE and maximum error for each system are provided in Table 2C-D. Since these parameters are

determined by regression, we note that they are averaged values that cannot obtain absolute agreement with every adsorption configuration considered in this study. Still, the average MAE across all systems was substantially reduced from 0.18 eV using only the monometallic parameters to just 0.13 eV using the re-optimized bimetallic parameters. The MAE corresponding to systems with bimetallic pairings across two columns of the periodic table was again the highest (> 0.15 eV); the remaining bimetallic pairings had an average MAE of just 0.08 eV. The increased errors for bimetallic pairings consisting of elements further apart in the periodic table hints that the d-electron screening is not as efficient, and that the error could be further reduced by including bond-specific compositional effects that are over and above the mean field approximation. These systems also exhibit very poor miscibility in experimental phase diagrams,[44] resulting in poor fits found using our parameterization procedure since they are not known to adopt an fcc-like intermixed alloy structure. We therefore do not focus much additional attention on these systems, since they likely do not correspond to systems that are as relevant for experimental bimetallic catalysis. When later demonstrating the transferability of our model to nanoparticles, we show that deviations of 1.7% (DEC) and 5.1% (ICO) in intraplanar distances from an ideal FCC stacking are tolerated within this framework.

For the remaining data points, a MAE of 0.08 eV represents a strong fit of the calculated adsorption energies to the parameterized model. This validates our underlying assumption that perturbations in coordination or composition around a site are largely confined to the first coordination shell, and generic morphological and local chemical environments are efficiently represented by explicitly considering atoms within the first coordination shell, hence, greatly reducing the number of fitted parameters required. Unlike the monometallic method we presented previously, in which 14 adsorption energies were used to determine 10 model

parameters, in this case at least 105 (up to 140) adsorption energies were used for determining the 20 model parameters for each bimetallic system, which minimizes the risk of overfitting our model. We anticipate that the minimum set of adsorption energies needed to parameterize the α_i^Z for new bimetallic systems should be substantially smaller than the 140 adsorption energies utilized for each bimetallic system in this study. The determination of that specific set is outside the scope of the present work; however, we briefly investigated the size of the training set by performing a non-exhaustive optimization of the set of geometries used to construct the α_i^Z parameters for each bimetallic combination (see ESI for more details). Considering the seven bimetallic combinations (Ag-Au, Ag-Pd, Au-Pd, Au-Pt, Pd-Pt, Ir-Rh, and Pt-Rh) for which no data points were discarded (due to reconstruction, etc.), we identify a training set of 70 out of 140 adsorption geometries that can determine α_i^Z parameters for all seven bimetallic systems with a MAE less than 0.10 eV across the entire data set (140 adsorption energies for each of 7 bimetallic combinations). While we make no claim about the global optimality of this data set, it suggests possible bounds for an ideal bimetallic training set in terms of error and number of calculations. Further optimization of the set would consider, e.g., data from larger unit cells and other mixed surface calculations, as discussed briefly in the following for the Pt-Pd bimetallic system. Finally, we also note that the exact values of the α_i^Z parameters are sensitive to calculation details such as the DFT functional and pseudopotential, though we anticipate that the general trends should be preserved regardless of these computational choices.

Table 2: Mean absolute error (MAE) and maximum absolute error in reconstructing adsorption energies from the bond-associated parameters in Table 1 to the corresponding bimetallic data sets: (A) MAE and (B) maximum error when using only the monometallic parameters to predict bimetallic data; (C) MAE and (D) maximum error when using the re-optimized parameters corresponding to each specific bimetallic system. All values are provided in eV.

A	Au	Cu	Ir	Pd	Pt	Rh
Ag	0.09	0.12	0.48	0.08	0.20	0.29
Au		0.12	0.43	0.09	0.13	0.20
Cu			0.23	0.12	0.20	0.11
Ir				0.21	0.14	0.08
Pd					0.14	0.11
Pt						0.12

B	Au	Cu	Ir	Pd	Pt	Rh
Ag	0.37	0.51	1.80	0.29	0.84	1.17
Au		0.79	1.46	0.38	0.55	0.71
Cu			1.05	0.39	0.80	0.47
Ir				0.75	0.54	0.32
Pd					0.48	0.34
Pt						0.45

C	Au	Cu	Ir	Pd	Pt	Rh
Ag	0.06	0.09	0.42	0.06	0.09	0.25
Au		0.10	0.35	0.07	0.09	0.15
Cu			0.19	0.11	0.14	0.08
Ir				0.15	0.07	0.06
Pd					0.05	0.08
Pt						0.05

D	Au	Cu	Ir	Pd	Pt	Rh
Ag	0.17	0.35	1.25	0.20	0.39	0.66
Au		0.66	0.99	0.25	0.36	0.38
Cu			0.90	0.33	0.42	0.31
Ir				0.57	0.29	0.25
Pd					0.16	0.21
Pt						0.19

Model Validation on Extended Surfaces of Pd-Pt Alloys

As a first test of the predictive power of the parameters derived from this model, we briefly evaluated adsorption energies for extended surfaces of Pd-Pt alloys (including Pt_3Pd and Pd_3Pt), which represent a system of two relatively miscible metals that are important components in a number of bimetallic heterogeneous catalysts.[45–47] We performed calculations using a 3x3 surface unit cell of (100) and (111) surface slabs, which allows for more arrangements of metal atoms with fewer restrictions imposed by the periodic boundary conditions. We considered metal adlayers having a coverage of up to 4/9 ML (4 atoms added to a 3x3 surface unit cell), since in our previous work we found those to correspond to the highest errors in predicted adsorption energies.[34] This yields a total of 912 adsorption energies for the Pt-Pd bimetallic system, considering all permutations of 1, 2, 3, or 4 atoms of Pt and/or Pd within the 3x3 unit cell constraints (772 adsorption energies) in combination with the originally-collected Pt and Pd data in the 2x2 unit cell (140 adsorption energies). Using the parameters optimized for the Pd-Pt bimetallic system shown in Table 1, we calculated a MAE for predicting adsorption energies in

the full Pd-Pt set of 0.09 eV (plotted in Figure 2A); the error in the original 140-point bimetallic

data set for this system was 0.05 eV. The adsorption energies with the largest error (> 0.40 eV)

correspond to adsorption on (111) slabs with triangular or diamond-like clusters of 3-4 metal

adatoms, as was the case for the monometallic Pd and Pt systems.[34] This phenomenon was

discussed in more detail in our previous work and can be attributed to inward relaxations of

surface atoms in those geometries and hence a significant increase in coordination for these

atoms that is not captured well by our parameterization procedure. We again note that our α_i^Z

parameters represent average values, and therefore perfect agreement with all arrangements of

atoms cannot be obtained using this simple energy scheme. Attempts at further re-optimization

of the 20 Pd-Pt parameters to include this expanded 3x3 surface data set in the parameterization

resulted in only minimal reduction of the MAE (reduced from 0.09 eV to 0.08 eV), reinforcing

this limitation of our model in capturing every possible configuration. Still, the accuracy

demonstrated by our method is sufficiently high to enable reliable simulation of nanoparticle

structures having different morphologies, sizes, and compositions, as we will demonstrate

subsequently.
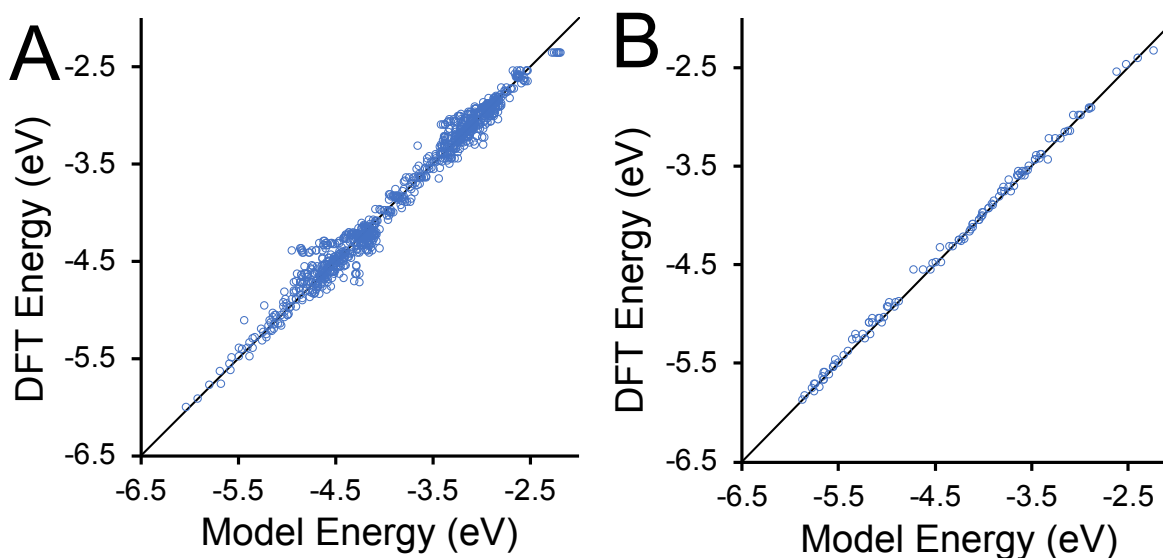
Figure 2: Comparison of model-predicted and DFT-calculated energies for Pt-Pd bimetallic systems: (A) 3x3 surface unit cells of (100) and (111) geometries (MAE 0.09 eV) and (B) 2x2 $Pd_3Pt(111)$ and $PdPt_3(111)$ unit cells (MAE 0.03 eV).

Since our model was parameterized considering adsorption of metals A and/or B on slabs of pure metal B, we also performed adsorption energy calculations on $Pd_3Pt(111)$ and $PdPt_3(111)$ alloy surfaces in 2 x 2 surface unit cells to briefly investigate the effect of heterogeneous surface composition on the model's ability to predict metal adsorption energies. This corresponds to an additional 112 Pd/Pt adsorption energies in cells with varying metal surface layer coverage. For these calculations, the unit cell was constructed with lattice constants interpolated between those of Pd and Pt, based on the surface composition (*i.e.*, using Vegard's law). In this case, the Pd-Pt bimetallic parameters predicted adsorption energies with a MAE of just 0.03 eV and a maximum error of 0.16 eV without any further optimization to the parameter set given in Table 1 (plotted in Figure 2B). This demonstrates the insensitivity of our model to surface composition.

Model Validation on Nanoparticles: Charge Accumulation on Subsurface Atoms

The primary target of our proposed model is to predict the energies of metal atoms in general configurations, such that we might ultimately predict the relative stability of different nanoparticle structures and understand the phenomena governing transformations between different structures. We note that, as in our previous work, we find substantial discrepancies between the calculated total energies of nanoparticles using DFT and using our model, on the order of 10-20 eV per particle (0.07 − 0.14 eV per atom). These discrepancies arise from finite-size effects: our model is parameterized using slab-based adsorption calculations, while the small nanoparticles exhibit considerable lattice contraction due to their small size. This effect was more thoroughly elucidated for the monometallic nanoparticles published in our previous work, including a series of fixed-lattice calculations to understand the nature of the finite size effects.[34]

19

Errors introduced by such finite-size effects can be swiftly eliminated while maintaining our simple coordination and composition based arguments by simply calibrating energies using best-fit lines as indicated in Figures 4, 5, and in the ESI. However, far more important than reproducing the total energy of nanoparticles is determining accurate relative energies of nanoparticle structures; these dictate the relative ease of transformations between structural arrangements.

We focus our analysis on accurately modeling these relative differences in small nanoparticles ($\sim 1.6 - 2.2$ nm), while noting that our predictions will become more accurate in the limit of larger nanoparticles as the slab models from which the α_i^Z parameters were derived become more representative of the nanoparticle structure. In this section, we will highlight the need for a robust scheme that corrects for destabilization induced by charge accumulation on second-layer atoms. Building on these insights, we will then introduce a correction scheme for this phenomenon, and subsequently utilize the refined model in predicting relative energies of nanoparticles having different morphologies, sizes, and compositions.

Our coordination-based model does not differentiate between configurations of atoms within the bulk of the nanoparticle, as all have the same coordination number and therefore possess no distinguishing features for different arrangements. As a first test of our model, we performed nanoparticle calculations with fixed monometallic shells and randomly arranged alloy cores of varying compositions. We initially focused on systems with Pt or Pd shells and Pt-Pd bimetallic cores. We first calculated the optimized structure of Pt and Pd monometallic particles; the 92 atoms in the outermost layer were then fixed at their optimized coordinates. The effect of shell relaxation on the relative nanoparticle energies for this series of calculations was found to be negligible for the Pd-Pt systems (differences in relative total energies of less than 0.02 eV).

We subsequently randomly substituted core atoms at 5 intermediate compositions ranging from

Pd-rich to Pt-rich and performed DFT calculations in which these core atoms were allowed to

fully relax. A schematic of these calculations is shown in Figure 3A. We note that these (and all

subsequent figures) present only the total energies of nanoparticles and no information about

configurational entropy; the latter could be determined in a relatively straightforward manner by

counting the number of equivalent structures.
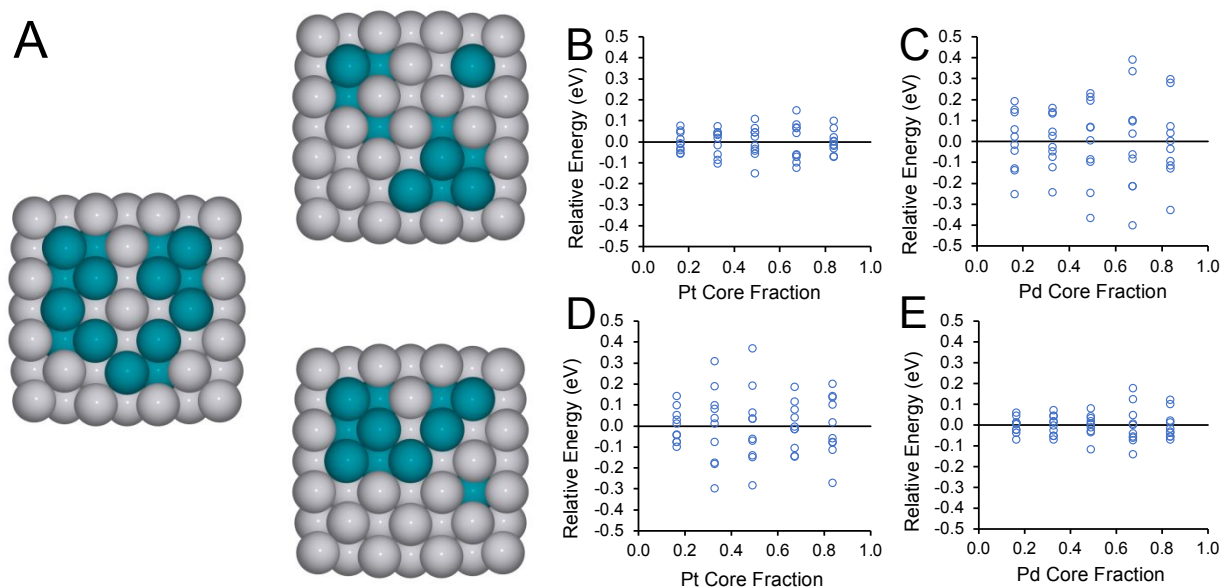
Figure 3: (A) Cross-sectional view of sample fixed-shell, variable-core calculations. The 92-atom shell (comprising only metal A) is fixed at its optimized nanoparticle coordinates, while the 55-atom core structure is randomly shuffled, and its composition varied. Pt and Pd atoms are depicted in grey and turquoise respectively. Plotted are the relative energies (per 55 atom shuffle) around the mean energy for each composition for (B) fixed Pd shell; (C) fixed Pt shell; (D) fixed Pd shell, Pt and Pd subsurface energies corrected separately, (E) fixed Pt shell, Pt and Pd subsurface energies corrected separately. To facilitate comparison, the mean energy for each Pt/Pd core fraction is realigned to 0.

We first considered the case in which all 55 atoms below the surface are treated as

completely interchangeable by the model; that is, we neglected all configurational effects for

atoms with 12-fold coordination, including second-shell corrections. In this case, we determine

the variations in DFT-calculated nanoparticle total energy as internal atomic arrangements

change and compare them to the model prediction that such rearrangements should have no change in energy. For the nanoparticle with the fixed Pd shell (Figure 3B), we found very small variations in nanoparticle total energy across Pd-Pt core compositions: the mean fluctuation of individual nanoparticle energies around the average total energy (realigned to 0 for each considered Pt or Pd core fraction) was 0.06 eV, which is a small value for a 55-atom mixing process. This fluctuation is one to two orders of magnitude smaller than the energies of Pt/Pd atomic swaps between the core and the surface (on the order of 0.1 eV/atom), which will be discussed subsequently. In contrast, the nanoparticle with a fixed Pt shell exhibited larger fluctuations around the mean energy for each composition (mean fluctuation 0.14 eV, Figure 3C). While these fluctuations are still reasonably small considering the number of atoms (55) intermixed internally, it was unexpected that there should be such a relatively large discrepancy in comparison with the Pd shell system, given that both systems involve intermediate internal compositions of a Pt-Pd alloy. As control calculations, we investigate energy changes in random Pd-Pt bulk structures (3x3x3 unit cell) at different internal compositions (see ESI for more details). As bulk atoms are shuffled at a given overall composition, we observe far lower fluctuations in relative energies of around 0.017 eV per 27 atom unit cell. This corroborates model predictions that enthalpy changes for shuffling bulk atoms in a bulk unit cell at a given composition are essentially zero and suggests that near-surface contributions are likely responsible for the model discrepancies. Thus, the unexpected fluctuations in energy shown in Figure 3 are unlikely to arise from the 13 atoms in the second and third subsurface layer (which closely represent atoms in the 3x3x3 bulk structures) but could stem from 42 atoms in the first sublayer being energetically dissimilar to bulk atoms.

The origin of this discrepancy is found by considering corrections to the energies of atoms in the first subsurface layer. As discussed in detail in our previous work, surface terminations of bulk structures result in the transfer of charge density from the surface layer to underlying layers.[34] This leads to a destabilization of atoms, particularly in the first subsurface layer; this destabilization is accounted for in our parameterization procedure by correcting the energy of atoms in the first subsurface layer by a fixed amount, depending on metal identity. From our previous work, the corrections on Pd and Pt atoms in the first subsurface layer were found to be 0.11 and 0.23 eV, respectively; we do not perform any direct re-optimization of these parameters in this work. Consideration of these simple energetic corrections in our model now enables it to distinguish between the internal configurations of 12-fold coordinated Pt and Pd atoms: of the 55 atoms in the core, 42 are located in the first subsurface layer. For a fixed core and shell composition, the relative energies of nanoparticles can thus be predicted by the relative amounts of Pt and Pd in that first subsurface layer according to the respective corrections to the two metals. We replotted the data in the Pt-shell, mixed Pt-Pd core system accounting for these corrections: for a fixed Pt-Pd 55-atom core composition, each additional Pt atom in the second layer is penalized by 0.12 eV (the difference between Pd and Pt corrections). This simple correction reduced the error of our predicted energies to just 0.05 eV around the mean (Figure 3E).

For consistency, we also applied this same correction scheme to the system with a Pd shell and mixed Pt-Pd core. This system demonstrated small fluctuations in total energy (averaging 0.06 eV around the mean) when subsurface corrections were not applied; large fluctuations averaging 0.11 eV were therefore seen when the separate Pt and Pd corrections were applied to the subsurface atoms (Figure 3D). This suggests that because of charge disruption

caused by dissimilar nearest neighbors, energy corrections to subsurface atoms are not necessarily straightforward in bimetallic systems: we must separately apply the Pt-derived second layer correction to Pt atoms and the Pd-derived correction to Pd atoms when they are located directly beneath a Pt shell (Figure 3E). The model predictions for systems with a Pd shell are, however, most accurate when we do not apply different corrections between Pt and Pd, and instead use the same value to correct the energy of subsurface Pd and subsurface Pt (Figure 3C). Thus, changing nearest neighbor identities around second layer Pt atoms from Pt to Pd results in electronic interactions between Pt and Pd that partially alleviates the destabilization effect caused by charge accumulation at the second layer Pt atoms. Although this correction scheme is developed for limiting scenarios of systems having a monometallic shell, we discuss its extension to random alloys with mixed Pd-Pt cores and shells in the next section.

While determining an exact rationale for this behavior is not within the scope of this current study (though it is potentially related to the extended 5d states in Pt compared with 4d states in Pd), this truly is a fine-tuning of the model since the fluctuations around the mean (~0.14 eV per 55 atom shuffling) are relatively small. Further, we are mostly interested in reliable predictions of surface energetics, which we examine more carefully in the subsequent sections and show to have a much broader energy range. We also briefly performed analogous variable-core, fixed-shell calculations for Cu-Rh, Pt-Au, and Cu-Au systems representing less ideal intermixing than the Pt-Pd case; important results are outlined in the ESI.

Model Validation on Nanoparticles: Effects of Morphology, Composition, and Size

Although it is desirable to describe all atomic shuffling processes with a high degree of accuracy, it is far more important from the perspective of catalysis to accurately represent

energetics near the catalyst surface. We therefore performed DFT calculations on nanoparticles having different morphologies (CUB, DEC, ICO, OCT), sizes (147 atom and truncated 309 atom clusters), and wide-ranging compositions. We examine the validity of our model towards predicting relative energies of nanoparticles, binding energies of metal atoms, and energetic changes of single atom swaps. Through these examples, we will illustrate the applicability of our framework to nanoparticles having slight deviations from an ideal FCC stacking.

We first consider idealized CUB structures with a core of metal B (55 atoms) and a monolayer shell of metal A (92 atoms), focusing initially on Pd-Pt and Pt-Pd core-shell structures. We then randomly shuffled all 147 atoms, yielding mixed Pd-Pt cores and shells, and evaluated their energies using DFT to determine how reliably our model predicts the relative energies of structures with variable surface compositions (example schematic shown in Figure 4A). The Pt/Pd nanoparticles also serve as a benchmark to compare our model with other approaches such as the effective medium theory[48] and the bond centric model[27]. Truly random core-shell arrangements result in roughly similar fractions of Pt and Pd in the core and shell across all arrangements of atoms, and our model predicts these to all fall within a similar energy range since energy differences are driven primarily by surface segregation of Pt and Pd. To avoid oversampling these particular energy ranges, we included additional shuffling in which fewer atoms were randomly exchanged between the 55-atom core and the 92-atom shell to specifically include sample compositions that fall in intermediate energy ranges.

In accordance with the results from the fixed-shell/variable core calculations in Figure 3, the energies of Pd and Pt atoms in the first subsurface layer must be corrected, depending on the surface composition. We found that Pd subsurface atoms should be corrected by the same amount, 0.11 eV, regardless of whether the surface layer consists of either pure Pt or pure Pd. On

the other hand, Pt subsurface atoms should be corrected by a larger amount (0.12 eV more) if the surface contains only Pt, and by the same amount as Pd subsurface atoms if the surface comprises only Pd. Extension of this scheme from systems having monometallic shells to those possessing mixed Pt-Pd surface composition therefore requires some additional consideration. Since the correction applied to subsurface Pd is the same in the presence of pure Pd and pure Pt overlayers, it follows that the same correction should be applied to Pd when it is located adjacent to some mixed fraction of Pd and Pt surface atoms. On the other hand, because of electronic interactions between Pt (subsurface layer) and Pd (surface) atoms, corrections to subsurface Pt atoms are dependent on the shell composition. We first attempted to determine these corrections using a linear scheme, in which the correction on a particular Pt atom was weighted by the fraction of its nearest-neighbor surface atoms that are Pd (x). The total correction on Pt subsurface atoms in this case was therefore calculated as $x * \alpha_{2nd}^{Pd} + (1 - x) * \alpha_{2nd}^{Pt}$.

We plot the results of these core-shell shuffling calculations in Figure 4B-C by considering a parity plot of predicted vs. calculated energies relative to the respective core-shell structures. A best-fit line for the respective shuffled data points (excluding the structures closest to the respective core-shell structures, which we will discuss subsequently) is also included. Ideally, this best-fit line would have unity slope and zero intercept to demonstrate perfect agreement between the model and DFT calculations (*i.e.*, falling exactly on the true parity line). Because these nanoparticles exhibit finite-size effects compared to the slab models used to parameterize the coordination-based model, slight deviations from unity slope and zero intercept are to be expected due to lattice contraction and strain. These effects are not directly captured by the model; we will discuss this in more detail later in the text. In the case of a linear correction to the subsurface Pt energies, we calculated best-fit slopes of 1.34 and 1.17 for the particles based

on Pt and Pd shells, respectively. The scatter of these data around the best-fit line was relatively

small for 147-atom cuboctahedral particles: the MAE from the best-fit line was 0.17 eV for the

Pt-shell and 0.14 eV for the Pd-shell references, respectively.
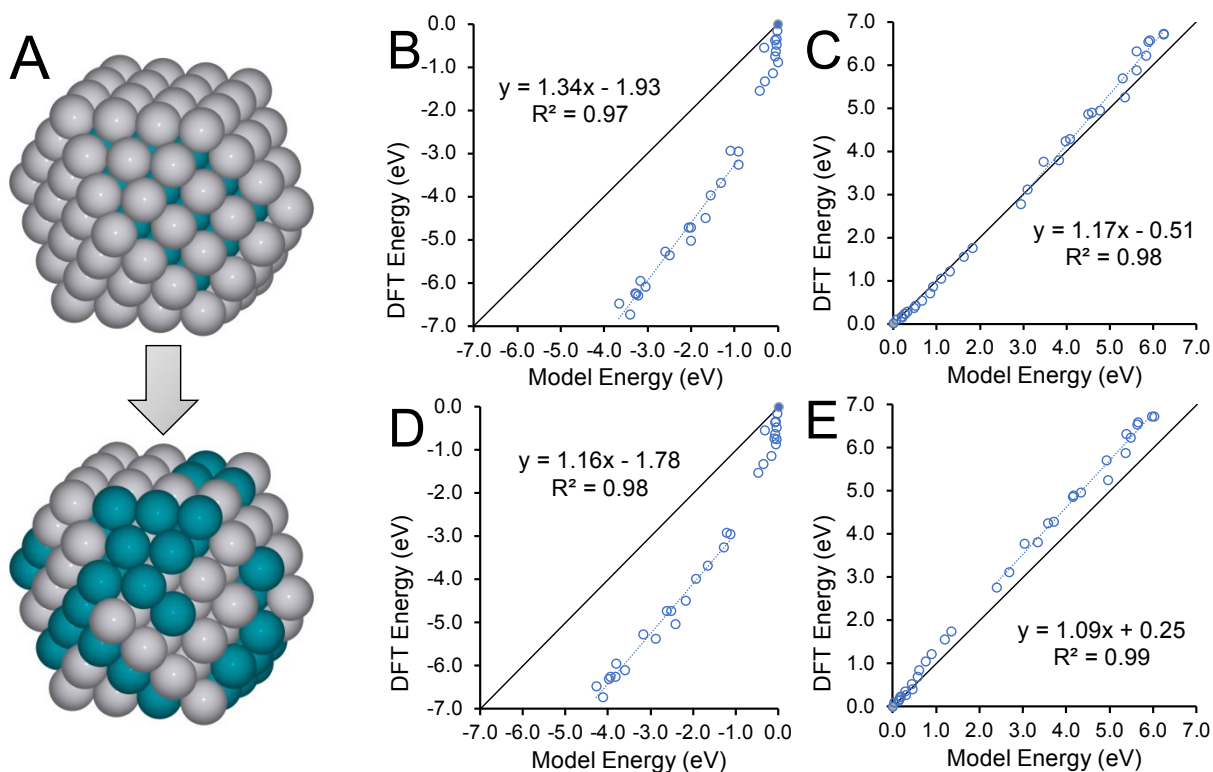
Figure 4: (A) Schematic of shuffling from a core-shell alloy structure to a randomly-ordered alloy structure. Pt and Pd atoms are depicted in grey and turquoise respectively. Comparison of model-predicted and DFT-calculated energies relative to core-shell structures using (B) Pd-Pt core-shell reference, $w = 1$ correction to subsurface energies; (C) Pt-Pd core-shell reference, $w = 1$ correction to subsurface energies; (D) Pd-Pt core-shell reference, $w = 1.93$; (E) Pt-Pd core-shell reference, $w = 1.93$.

The nature of the second-layer correction dependence on shell composition and

subsurface atom identity suggests that a linear correction may not be the most suitable approach.

We performed a data exercise to determine the correction scheme that provides the most optimal

relative energies between the various nanoparticle configurations. We chose to introduce a

correction factor y that is nonlinear in composition, such that $y = (1 - x)^w$ for some positive

value w. We then calculate the total correction on Pt subsurface atoms as $(1 - y) * \alpha_{2nd}^{Pd} + y * \alpha_{2nd}^{Pt}$. We note that the linear correction described previously corresponds to the case in which $w = 1$ (Figures 4(B) and 4(C)), and that a case in which subsurface Pt corrections are treated independently of surface composition (*i.e.* Pt is assigned only its own correction factor determined from the monometallic parameterization) corresponds to $w = 0$, the limiting scenario discussed in Figure 3(E). We varied w to determine the value that minimizes the MAE and found that $w = 1.93$ yielded MAE of 0.15 eV and 0.12 eV around the respective best-fit lines for the systems based on the Pt and Pd shells (Figure 4D-E). The respective slopes of the resulting linear relationships were also closer to unity (1.16 and 1.09 eV, respectively). We note that the overall compositions of nanoparticles in the training set ($Pt_{55}Pd_{92}$ or $Pt_{92}Pd_{55}$) has negligible impact on the fitted coefficient of 1.93 thereby indicating that the exponent is species dependent and not strongly influenced by the overall composition. Furthermore, we will later show that this coefficient is directly transferable across Pt/Pd nanoparticles having wide-ranging overall compositions (Pt rich to Pd rich), morphologies, and sizes, reinforcing the local nature of this correction. Such a conclusion is not unexpected, given the strong d-electron screening prevalent beyond the first coordination shell. The nonlinear nature of this correction (1.93) indicates that progressive replacement of surface Pt atoms with Pd acutely reduces the destabilization caused by charge accumulation on second layer Pt atoms hinting at a synergistic electronic interaction between Pt and Pd.

As we discussed previously, we anticipated that slight deviations from ideal behavior would arise from finite-size effects; these effects should diminish in larger systems. Still, the small errors in the relative energies between particles suggest that this approach is useful even for determining the energies of small nanoparticles such as in this study. Furthermore, the parity

plots reveal that while total energy predictions from our model deviate from the parity line, relative energies corresponding to single atom swaps will correspond more closely to DFT derived energies. These relative changes represent, for example, thermodynamics of elementary steps in a particle migration model, and are more directly related to catalysis applications than are the total energies of nanoparticles. A parity plot, contrasting DFT and model predictions for single atom swaps will be discussed subsequently in Figure 5. A direct comparison of our model predictions (Figure 4) to alternative approaches is illustrated in the ESI.

When examining the data for the optimized model (*i.e.* Figure 4D-E), we note that the data for the case based on the Pt shell (Figure 4D) are still noticeably offset from the parity line. This offset appears to originate from strain present in the core-shell structure. The data points closest to the high-energy core-shell structure, which is plotted as the zero-energy reference, fall sharply in energy compared to the structure with the pure Pt shell as Pd atoms are introduced one-by-one into various surface sites in the shell. This sharp release in energy explains the large magnitude of the best-fit intercept shown in Figure 4D: once a total of 6-7 Pd atoms have been introduced into the 92-atom Pt shell, the energy curve then adopts a slope similar to that of the more stable structures at lower energy ranges. The exact origin of this strain effect is beyond the scope of the present study, though we note it is not prominent in the case of the more stable Pd shell (Figure 4E), as the best-fit line shows a nearly zero intercept. This represents a limitation of our model, although we note that it does capture the desired features of physically favorable structures (the perfect Pt shell is both energetically and entropically unfavorable). We performed similar studies on the Au-Cu bimetallic system (see ESI), finding that the model is qualitatively accurate in predicting relative energies though exhibits a larger degree of scatter as anticipated due to the large size mismatch of Au and Cu atoms and their strong preference to form well-

ordered alloys to minimize strain. Still, the overall accurate representation of relative surface atom preferences (*i.e.* segregation) is the most important feature of our model, even for bimetallic systems lacking idealized fcc stacking, since the atoms nearest the surface are most relevant for practical investigations in heterogeneous catalysis.

Following our analysis of cuboctahedral nanoparticles, we examine the transferability of our model to nanoparticles having different morphologies (OCT, DEC, ICO), sizes (147 atom and truncated 309 atom), and compositions (Pt rich to Pd rich). We choose DEC and ICO structures to investigate the validity of our model in the presence of deviations in intraplanar bonds (1.7% for DEC and 5.1% for ICO) from an ideal FCC stacking. Model predictions with the 147 atoms, truncated 309 atoms, and extended surfaces are compared to qualitatively understand the impact of finite size effects on total and relative energies. A detailed discussion about morphological and compositional variations is presented in the ESI. Cohesive energy predictions for PtPd nanoparticles having progressively varying compositions from Pt rich to Pd rich are in good agreement with DFT derived energies. More crucially, relative energies of nanoparticles (referenced to monometallic Pd) having varying compositions have an even better agreement with a MAE of 0.005 eV per atom. This clearly indicates that our model describes compositional variations that can occur during segregation or sintering with a high degree of accuracy. We next investigate the impact of nanoparticle morphology, specifically focusing on DEC and ICO structures that deviate from an ideal FCC stacking. Despite intraplanar distortions of 1.7% and 5.1% for DEC and ICO, binding energies of metal atoms are predicted within 0.19 eV which is comparable to the errors on CUB nanoparticles. Nanoparticle cohesive energies also display similar errors between CUB (0.15 eV per atom) and ICO, DEC (0.16 eV per atom)

indicating that despite mild structural distortions, our distance independent framework is still valid. Further details are presented in the ESI.

The final set of DFT nanoparticle calculations investigates the accuracy of our model in predicting the energies of selected single-atom swaps, which is of most relevance to future studies related to understanding catalyst dynamics with atom-by-atom precision. We consider nanoparticles having varying morphologies, sizes, and compositions as listed in the preceding paragraph. We here implement the subsurface correction scheme in which the composition was numerically optimized as described previously for the Pt-Pd CUB system ($w = 1.93$). A full accounting of all considered swaps and associated energies is tabulated in the ESI. In general, these consisted of swaps between atoms in the core, between the 1st and 2nd subsurface layers, between the surface and 1st subsurface layer, and between surface sites. The calculated MAE of the 42 atomic swaps was just 0.05 eV, with a maximum error of 0.16 eV. Further details about initial and final states are provided in the ESI. Larger errors also correspond to a swap between the central core atom and an atom in the 2nd subsurface layer in the Pt_3Pd system, which is predicted by the model to have zero energy change but has a DFT-calculated 0.13 eV energy cost (Figure 5). We note that there are several other swaps with model-predicted energy 0.0 eV that reflect small variations in DFT energy as observed for our shuffling studies (Figure 3). Our model does not include any corrections to account for such behaviors deep in the nanoparticle core, but we envision that future refinements could aid our understanding of such behaviors. We briefly discuss the influence of finite size effects by comparing energy changes of single atom swaps on 147 atom and truncated-309 atom (half-309) nanoparticles. With increasing terrace sizes, we note a modest improvement in the MAE from 0.05 eV (147 atom) to 0.02 eV (half-309). In the limit of infinitely large terraces on periodic slabs (Figure 2), we see an error of 0.03

eV for Pt$_3$Pd and Pd$_3$Pt slabs. These results clearly indicate that the fidelity of our framework is enhanced with increasing nanoparticle size. We again emphasize the importance in catalytic contexts of obtaining correct energies for atomic movements at the surface and believe that the high model accuracy corresponding to these swaps demonstrates the effectiveness of our model for future studies in heterogeneous catalysis.
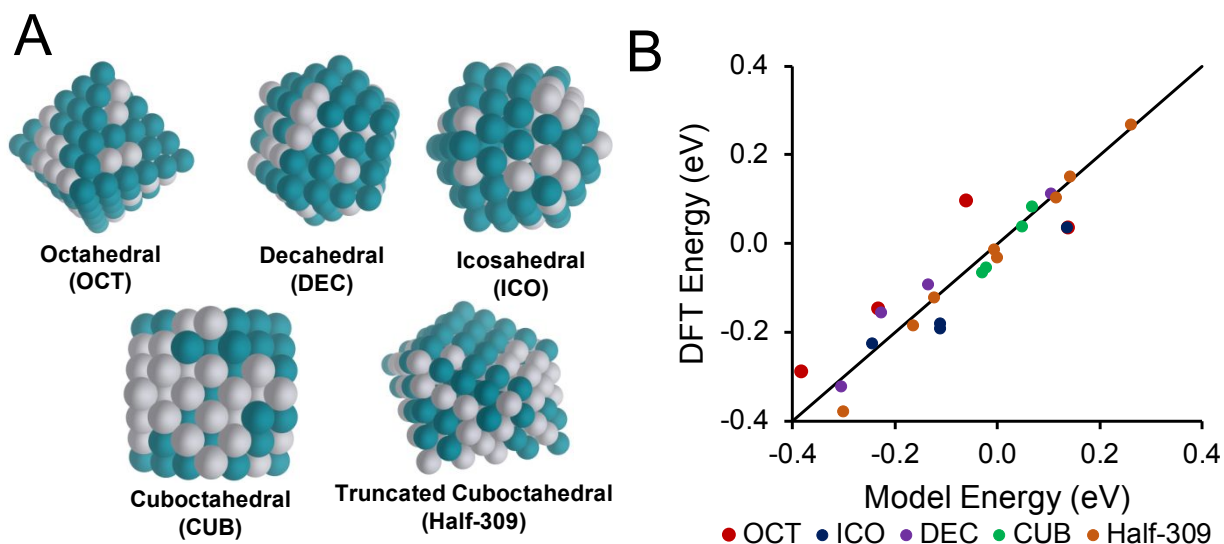
Figure 5: (A) Schematics of PtPd alloy nanoparticles considered for single-atom swaps in this study. Pt and Pd atoms are depicted in grey and turquoise respectively. (B) Comparison of model-predicted and DFT-calculated energies of single-atom swaps in these structures.

Comparisons with Existing Alloy Stability Models and Broader Impact

We briefly compare our coordination-based approach to existing models in the literature in terms of accuracy, transferability, parameter space, and computational cost. We then highlight future extensions needed to better describe small nanoparticles (below ~ 1.6 nm) having significant finite size and strain effects and conclude by discussing the broader impact of our model in engineering the next generation of bimetallic alloys that are designed with atomic level precision.

Our coordination-based model utilizes a small set of bond-associated parameters (10 per element) to wholly describe nanoparticle energies. These assumptions are founded on the "near-sightedness" in transition metals wherein perturbations in coordination and composition rapidly decay beyond the first coordination shell.[33] Our rigorous comparison of model predictions with DFT calculations in Table 2 and Figures 2-5 reveals a mean average error in the region of 0.10 to 0.15 eV per atom. Here, we summarize a comparison between our approach and alternative models including the effective medium theory[48], bond centric model (BCM)[27], Bayesian linear regression[18,19], and cluster expansions[20]. Trends in cohesive and relative energies of PdPt nanoparticles as a function of local chemical composition are better described using α_i^Z parameters in comparison with either EMT or BCM, with the latter approaches overestimating cohesive energies. A more detailed discussion is provided in the ESI. Unlike EMT or BCM which rely on a small number of fitted parameters (7 and 2 respectively), Bayesian linear regression and cluster expansions have a significantly larger parameter space which also require a greater number of DFT calculations (800 and 107 respectively) in the training set. This enhanced flexibility in parameter space yields predicted cohesive energies with an error below 0.02 eV per atom but makes reparameterizations for new bimetallic pairing computationally intensive. Our method uses parameters (20) based on simple slab models across 21 bimetallic pairings and predicts cohesive energies within 0.15 eV per atom for 147 atom nanoparticles. We anticipate the accuracy to improve with increasing nanoparticle size as finite and quantum size effects diminish. We believe that our coordination-based model, which exploits well known screening effects in transition metals, represents an effective compromise between accuracy and size of parameter space and can efficiently screen alloy stabilities across a wide range of morphology and local chemical ordering.

We finally discuss some limitations of our model and future extensions that may be needed to maximize its utility in describing heterogeneous catalysts. First, since this model is based entirely on atomic coordination and parameterized by a series of slab-based surface calculations it is unable to capture finite-size strain effects characteristic of small nanoparticles. Such effects typically have a destabilizing effect on adsorption energies (as was shown in our previous works for metal and molecular adsorption).[34,49] The impact of compressive strain on metal atom stabilities has a clear dependence on the metal coordination number. We show that compressive strain has a stronger influence on stabilities of nine-coordinated atoms on (111) terraces in comparison to low-coordinated corner atoms. A detailed discussion along with a comparison between model predicted and DFT derived adsorption energies is presented in the ESI. These results are consistent with a rigorous study by Li and coworkers who report strong surface tension effects on 147 (1.6 nm) atom Pt nanoparticles.[49] Accurate descriptions of nanoparticles having sizes below 1.6 nm require systematic treatments of both finite and quantum size effects, which is beyond the scope of our paper.[49–51] An implication of these effects is that our model becomes more accurate as nanoparticles become larger and more representative of the extended surface calculations used to parameterize the model; deviations from ideality, such as the non-unity slopes shown in Figure 4D-E, will be present in smaller nanoparticles as in this study. One could envision a possible correction scheme in which the corresponding α_i^Z parameters could be adjusted according to the observed contraction of a nanoparticle. This remains a somewhat abstract concept, since such relaxations will be dependent on the nanoparticle shape and local environment of each atom. Still, the DFT calculations associated with such corrections should remain tractable since the corrections are most relevant for small system sizes. Alternatively, model predictions using α_i^Z parameters for such special cases can be

calibrated to a limited set of DFT calculations using best fit lines as shown in Figure 4 and in the ESI. The latter approach retains the simple formulation of our coordination-based model while almost entirely eliminating errors induced by finite size effects.

In addition to whole-particle strain effects, this study also underscores the importance of understanding localized strain effects in bimetallic systems of atoms with highly disparate sizes (*e.g.*, Au and Cu, as outlined in the ESI). While the present study does not make any corrections that would describe the formation of well-ordered bulk phases (such as in the Au-Cu systems), we again note that our primary goal is an accurate representation of surface atom energies, as these are most relevant for sintering as well as catalysis applications. While we anticipate future refinements to the model that will account for effects of nearest-neighbor identity to more accurately describe well-ordered systems such as Au-Cu, we note that even for Au-Cu systems we are able to reproduce the relative energies of different surface terminations in nanoparticle models and therefore the model will have the ability to describe catalytic processes if these energies are treated accurately. Future work may also yield a more refined approach to treating the corrections on atoms in the first subsurface layer, which were not treated in detail in this study. It is somewhat more important to understand these subsurface effects on the energetics in better detail than bulk properties, since they directly affect surface atom stability and thereby their reactivity toward intermediates in catalytic reactions.

In principle, an extension of these coordination-based arguments to predict kinetics of atomic motion should be a straightforward concept. In practice, it is somewhat difficult to precisely define the coordination numbers of atoms located at transition states, since they involve atoms moving off fcc lattice sites to, *e.g.*, bridge sites, and therefore exhibit varying degrees of partial coordination to surface atoms. As shown in this work, however, a monometallic model for

the kinetics of atomic diffusion should have a relatively straightforward extension to bimetallic systems simply by tracking associated changes in coordination number for each metal type. Understanding and generalizing this model to include activation barriers of diffusion processes will enable direct extensions to dynamic simulations of phenomena such as sintering of multi-metallic systems.[35]

Finally, we again mention that the presence of catalytic intermediates can dramatically alter the segregation of metal components near the surface, and that extensions of this bimetallic coordination model to real catalytic systems must account for these phenomena. This will require a great deal of further investigation, though we note in principle the possibility of coupling with a model such as the one we derived for monometallic systems, in which adsorption energies of metal atoms can directly predict adsorption energies of catalytic intermediates.[36] Such a scheme will not only reveal surface dynamics at a site-by-site specificity, but in conjunction with the coordination-based model can also be integrated with volcano-based screening paradigms, creating a powerful framework for reverse engineering targeted active site ensembles on bimetallic catalysts with atomic resolution.

Conclusions

In this work, we have presented a general scheme for predicting metal atom adsorption energies for bimetallic systems that is based on their nearest-neighbor coordination number with compositional effects considered through a mean field approximation. We showed that a series of simple slab-based calculations reliably parameterizes a model that predicts relative energies of both extended surfaces and nanoparticles with accuracies within 0.15 eV. By exploiting strong screening effects of d-electrons, we reveal that a remarkably limited set of parameters (10 for

each element) can represent an expansive morphological and compositional space across bimetallic alloys. The model is particularly adept at describing surface and near-surface phenomena, which is essential for its potential use in catalyst design applications. In a broader context, it also accurately predicts relative energies of nanoparticles with different atomic arrangements across wide ranging morphologies, sizes (above 1.6 nm), and composition. We further anticipate that coupling this bimetallic model with an adsorption model similar to that found for monometallic systems opens the possibility of efficient catalyst screening and design. While we suggest further refinements to the model to capture the fine details of bulk ordering and immiscible systems, the accurate prediction offered by the methods presented will prove a valuable tool in understanding the ordering of bimetallic heterogeneous catalysts.

Conflicts of Interest

There are no conflicts to declare.

Footnotes

Electronic Supplementary Information is available. All data generated by this study are maintained in the SUNCAT Catalysis Hub database located at www.catalysis-hub.org.

References

1 D. Wang and Y. Li, *Adv. Mater.*, 2011, **23**, 1044–1060.

2 M. Sankar, N. Dimitratos, P. J. Miedziak, P. P. Wells, C. J. Kiely and G. J. Hutchings, *Chem. Soc. Rev.*, 2012, **41**, 8099–8139.

3 A. K. Singh and Q. Xu, *ChemCatChem*, 2013, **5**, 652–676.

4 J. B. Miller, C. Matranga and A. J. Gellman, *Surf. Sci.*, 2008, **602**, 375–382.

5 S. Zafeiratos, S. Piccinin and D. Teschner, *Catal. Sci. Technol.*, 2012, **2**, 1787–1801.

6 R. Ferrando, J. Jellinek and R. L. Johnston, *Chem. Rev.*, 2008, **108**, 845–910.

7 V. Ponec, *Appl. Catal. A-General*, 2001, **222**, 31–45.

8 A. V Ruban, H. L. Skriver and J. K. Norskov, *Phys. Rev. B*, 1999, **59**, 15990–16000.

9 A. U. Nilekar, A. V Ruban and M. Mavrikakis, *Surf. Sci.*, 2009, **603**, 91–96.

10 L. T. Roling and M. Mavrikakis, *Nanoscale*, 2017, **9**, 15005–15017.

11 Y. Han, D.-J. Liu and J. W. Evans, *Nano Lett.*, 2014, **14**, 4646–4652.

12 A. L. Gould, C. J. Heard, A. J. Logsdail and C. R. A. Catlow, *Phys. Chem. Chem. Phys.*, 2014, **16**, 21049–21061.

13 L.-L. Wang and D. D. Johnson, *J. Am. Chem. Soc.*, 2009, **131**, 14023–14029.

14 G. Barcaro, A. Fortunelli, M. Polak and L. Rubinovich, *Nano Lett.*, 2011, **11**, 1766–1769.

15 J. R. Boes and J. R. Kitchin, *J. Phys. Chem. C*, 2017, **121**, 3479–3487.

16 S. Hajinazar, J. Shao and A. N. Kolmogorov, *Phys. Rev. B*, 2017, **95**, 14114.

17 N. Artrith and A. M. Kolpak, *Nano Lett.*, 2014, **14**, 2670–2676.

18 R. Jinnouchi and R. Asahi, *J. Phys. Chem. Lett.*, 2017, **8**, 4279–4283.

19 R. Jinnouchi, H. Hirata and R. Asahi, *J. Phys. Chem. C*, 2017, **121**, 26397–26405.

20 J. Teeriniemi, M. Melander, S. Lipasti, R. Hatz and K. Laasonen, *J. Phys. Chem. C*, 2017,

121, 1667–1674.

21   S. Heiles and R. L. Johnston, *Int. J. Quantum Chem.*, 2013, **113**, 2091–2109.

22   N. S. Froemming and G. Henkelman, *J. Chem. Phys.*, , DOI:10.1063/1.3272274.

23   T.-D. Liu, L.-Y. Xu, G.-F. Shao, N.-N. Tu, J.-P. Tao and Y.-H. Wen, *J. Alloys Compd.*, 2016, **663**, 466–473.

24   A. Bruma, R. Ismail, L. O. Paz-Borbon, H. Arslan, G. Barcaro, A. Fortunelli, Z. Y. Li and R. L. Johnston, *Nanoscale*, 2013, **5**, 646–652.

25   G. Rossi and R. Ferrando, *J. Phys. Condens. Matter*, , DOI:10.1088/0953-8984/21/8/084208.

26   T. L. Tan, L.-L. Wang, D. D. Johnson and K. Bai, *Nano Lett.*, 2012, **12**, 4875–4880.

27   Z. Yan, M. G. Taylor, A. Mascareno and G. Mpourmpakis, *Nano Lett.*, 2018, **18**, 2696–2704.

28   W. Chen, W. F. Schneider and C. Wolverton, *J. Phys. Chem. C*, 2014, **118**, 8342–8349.

29   I.-H. Svenum, J. A. Herron, M. Mavrikakis and H. J. Venvik, *Catal. Today*, 2012, **193**, 111–119.

30   F. Tao, M. E. Grass, Y. Zhang, D. R. Butcher, J. R. Renzas, Z. Liu, J. Y. Chung, B. S. Mun, M. Salmeron and G. A. Somorjai, *Science (80-.).*, 2008, **322**, 932–934.

31   P. L. Hansen, J. B. Wagner, S. Helveg, J. R. Rostrup-Nielsen, B. S. Clausen and H. Topsøe, *Science (80-.).*, 2002, **295**, 2053–2055.

32   A. Dhouib and H. Guesmi, *Chem. Phys. Lett.*, 2012, **521**, 98–103.

33   J. K. Nørskov, T. Bligaard, B. Hvolbæk, F. Abild-Pedersen, I. Chorkendorff and C. H. Christensen, *Chem. Soc. Rev.*, 2008, **37**, 2163–2171.

34   L. T. Roling, L. Li and F. Abild-Pedersen, *J. Phys. Chem. C*, 2017, **121**, 23002–23010.

35   L. Li, P. N. Plessow, M. Rieger, S. Sauer, R. S. Sanchez-Carrera, A. Schaefer and F. Abild-Pedersen, *J. Phys. Chem. C*, 2017, **121**, 4261–4269.

36   L. T. Roling and F. Abild-Pedersen, *ChemCatChem*, 2018, **10**, 1643–1650.

37   P. Giannozzi, S. Baroni, N. Bonini, M. Calandra, R. Car, C. Cavazzoni, D. Ceresoli, G. L. Chiarotti, M. Cococcioni, I. Dabo, A. Dal Corso, S. De Gironcoli, S. Fabris, G. Fratesi, R. Gebauer, U. Gerstmann, C. Gougoussis, A. Kokalj, M. Lazzeri, L. Martin-Samos, N. Marzari, F. Mauri, R. Mazzarello, S. Paolini, A. Pasquarello, L. Paulatto, C. Sbraccia, S. Scandolo, G. Sclauzero, A. P. Seitsonen, A. Smogunov, P. Umari, R. M. Wentzcovitch and P. Giannozzi, *J. Phys. Condens. Matter*, 2009, **21**, 395502.

38   B. Hammer, L. B. Hansen and J. K. Nørskov, *Phys. Rev. B*, 1999, **59**, 7413–7421.

39   D. Vanderbilt, *Phys. Rev. B*, 1990, **41**, 7892–7895.

40   A. Hjorth Larsen, J. Jørgen Mortensen, J. Blomqvist, I. E. Castelli, R. Christensen, M. Dułak, J. Friis, M. N. Groves, B. Hammer, C. Hargus, E. D. Hermes, P. C. Jennings, P. Bjerre Jensen, J. Kermode, J. R. Kitchin, E. Leonhard Kolsbjerg, J. Kubal, K. Kaasbjerg, S. Lysgaard, J. Bergmann Maronsson, T. Maxson, T. Olsen, L. Pastewka, A. Peterson, C. Rostgaard, J. Schiøtz, O. Schütt, M. Strange, K. S. Thygesen, T. Vegge, L. Vilhelmsen, M. Walter, Z. Zeng and K. W. Jacobsen, *J. Phys. Condens. Matter*, 2017, **29**, 273002.

41   W. M. Haynes, Ed., *CRC Handbook of Chemistry and Physics*, CRC, Boca Raton, 2016.

42   L. Bengtsson, *Phys. Rev. B*, 1999, **59**, 12301–12304.

43   H. J. Monkhorst and J. D. Pack, *Phys. Rev. B*, 1976, **13**, 5188–5192.

44   T. B. Massalski, *Binary Alloy Phase Diagrams*, II., 1990, vol. 1.

45   H. S. Gandhi, G. W. Graham and R. W. McCabe, *J. Catal.*, 2003, **216**, 433–442.

46   K. Persson, A. Ersson, K. Jansson, J. L. G. Fierro and S. G. Jaras, *J. Catal.*, 2006, **243**,

14–24.

47   T. R. Johns, J. R. Gaudet, E. J. Peterson, J. T. Miller, E. A. Stach, C. H. Kim, M. P. Balogh and A. K. Datye, *ChemCatChem*, 2013, **5**, 2636–2645.

48   K. W. Jacobsen, P. Stoltze and J. K. Nørskov, *Surf. Sci.*, 1996, **366**, 394–402.

49   L. Li, F. Abild-Pedersen, J. Greeley and J. K. Nørskov, *J. Phys. Chem. Lett.*, 2015, **6**, 3797–3801.

50   L. Li, A. H. Larsen, N. A. Romero, V. A. Morozov, C. Glinsvad, F. Abild-Pedersen, J. Greeley, K. W. Jacobsen and J. K. Nørskov, *J. Phys. Chem. Lett.*, 2013, **4**, 222–226.

51   J. Kleis, J. Greeley, N. A. Romero, V. A. Morozov, H. Falsig, A. H. Larsen, J. Lu, J. J. Mortensen, M. Dułak, K. S. Thygesen, J. K. Nørskov and K. W. Jacobsen, *Catal. Letters*, 2011, **141**, 1067–1071.